Composites: Part A 204 (2026) 109610

Contents lists available at ScienceDirect

Composites Part A

journal homepage: www.elsevier.com/locate/compositesa

Integrating ReaxFF-MD simulations into fire safety performance evaluation of polypropylene/ammonium polyphosphate composites

Chunxiao Liu [a], Benjamin Tawiah [b], Anthony Chun Yin Yuen [a,*], Qian Chen [c], Ivan Miguel De Cachinho Cordeiro [d], Yuxin Zhang [a], Liming Jiang [a]

[a] Department of Building Environment and Energy Engineering, The Hong Kong Polytechnic University, Hong Kong, China
[b] School of Fashion and Textiles, The Hong Kong Polytechnic University, Hung Hom, Kowloon, Hong Kong Special Administrative Region
[c] Department of Architecture and Civil Engineering, City University of Hong Kong, Hong Kong, China
[d] School of Mechanical and Manufacturing Engineering, University of New South Wales, Sydney, NSW 2052, Australia

ARTICLE INFO

Keywords:
Ammonium polyphosphate
Condensed-phase mechanism
Flame retardancy
Polypropylene composites
Polymerisation degree
ReaxFF-MD

ABSTRACT

Polypropylene (PP) is widely used in consumer and engineering applications but is highly flammable and prone to melt-dripping. Here, we investigate how the polymerisation degree and water solubility of ammonium polyphosphate (APP) control the fire behaviour of PP/APP composites, combining UL-94, limiting oxygen index (LOI) and cone calorimetry with TG-FTIR, tensile testing and multi-scale morphology/chemistry characterisation (SEM/EDS, Raman and XPS) and ReaxFF reactive molecular dynamics (ReaxFF-MD) simulations. Two APP grades are examined: a highly polymerised, poorly soluble APP (WR-APP) and a low-polymerised, water-soluble APP (WP-APP). The fire tests show that WR-APP attains higher LOI values and UL-94V-0 ratings at lower loadings, forms denser P/N-rich char layers and reduces smoke production, whereas WP-APP leaves porous residues and requires higher loadings to reach comparable performance. SEM of unburned composites indicates APP-related accumulations and pull-out cavities, which become more evident at higher loadings and are consistent with the loss of ductility/strength in tensile tests. ReaxFF-MD simulations further show that WR-APP extends the induction period of PP pyrolysis, delays hydrocarbon release and promotes phosphate-mediated char-network formation, consistent with a delayed and localised decomposition process. TG-FTIR provides experimental support by tracking the evolution of key volatile species, strengthening the micro–macro linkage between simulated product trends and measured fire behaviour. Relating these atomistic results to the macroscopic fire behaviour underscores the roles of APP polymerisation degree and solubility in the condensed-phase flame-retardant action of PP and provides guidance for optimising halogen-free flame retardants for polyolefin systems.

1. Introduction

Polypropylene (PP) is widely used in automotive interiors, electrical housings and building components owing to its low cost, ease of processing and balanced mechanical properties [1–3]. However, its inherent flammability and melt-dripping during combustion lead to rapid heat release and secondary ignition of adjacent materials, which limits its use in applications with strict fire-safety requirements [4–7]. These hazards are of particular concern in transport and building sectors, where regulations such as UNECE R118 for automotive interiors and EN 45545 for railway materials specify minimum fire performance levels [8–11]. Consequently, there is a clear need for flame-retardant approaches that improve the fire behaviour of PP while retaining its processing and cost advantages.

Among halogen-free flame-retardant systems, ammonium polyphosphate (APP) is widely used because it promotes char formation in the condensed phase and can act as a radical scavenger in the gas phase [12–16]. As the typical acid source in intumescent flame retardants (IFRs), APP has been incorporated into many thermoplastic matrices, often together with pentaerythritol (PER), melamine or inorganic fillers to improve flame-retardant efficiency and processing [17–21]. Most of these studies focus on formulation design through synergists, surface modification or microencapsulation of APP. In contrast, the influence of the intrinsic parameters of APP itself—such as polymerisation degree

* Corresponding author.
E-mail address: anthony-cy.yuen@polyu.edu.hk (A.C.Y. Yuen).

https://doi.org/10.1016/j.compositesa.2026.109610
Received 23 November 2025; Received in revised form 15 January 2026; Accepted 28 January 2026
Available online 29 January 2026

and water solubility—on the flame-retardant behaviour of PP has been much less systematically explored. Existing reports mainly provide isolated examples, for instance improved water resistance and smoke suppression via surface-engineered APP [22], or denser char structures induced by carbonaceous or inorganic co-additives [23,24], but do not establish how APP structure controls the underlying condensed-phase mechanisms.

The roles of intrinsic APP features—particularly polymerisation degree and water solubility, together with the effective loading—in controlling PP anti-dripping, char formation and smoke/toxicity reduction are still not well quantified. Highly polymerised APP can facilitate the formation of continuous polyphosphate networks but tends to disperse poorly in PP matrices [2,3,25], while lower-polymerisation, more water-soluble APP is prone to migration and loss of performance during service [26,27]. How these structural characteristics combine to determine the condensed-phase flame-retardant mechanisms of APP in PP, and how they can be translated into quantitative design rules, remains insufficiently established.

Beyond uncertainties in APP structure–property relationships, a further challenge is linking molecular-level degradation processes to macroscopic fire-performance metrics. Conventional UL-94 and LOI tests provide rapid classification of flame retardancy but do not resolve the relative roles of gas-phase and condensed-phase mechanisms, while cone calorimetry yields global parameters such as peak and total heat release without directly capturing radical evolution or char build-up [28–30]. Advanced spectroscopic and thermal analysis techniques, including TG-FTIR, Raman spectroscopy, XPS and synchrotron-based methods, have improved our ability to identify degradation products and char microstructures in flame-retardant systems [31–33], yet these measurements typically offer single-scale views and are not routinely integrated into a cross-scale mechanistic framework. In fire field modelling that includes solid pyrolysis, reliable kinetic parameters are required for the underlying materials, particularly when flame retardants are present [34,35]. Reactive force-field molecular dynamics (ReaxFF-MD) can simulate concurrent bond breaking/formation and radical reactions during polymer degradation, providing atomistic insight into pyrolysis and char nucleation processes [36,37]. Several recent studies on HDPE/APP, EPS and EVA-based composites have shown that ReaxFF simulations can reproduce trends in pyrolysis kinetics and char formation that are consistent with experimental indicators such as LOI, UL-94 ratings and cone calorimetry metrics [38–40]. In this sense, ReaxFF-MD is well suited to provide comparative atomistic insight that helps rationalise trends in macroscopic fire behaviour [41,42]. However, systematic schemes that integrate ReaxFF-MD outputs with standard fire-performance tests to construct experimentally testable micro–macro linkages for APP-filled PP systems are

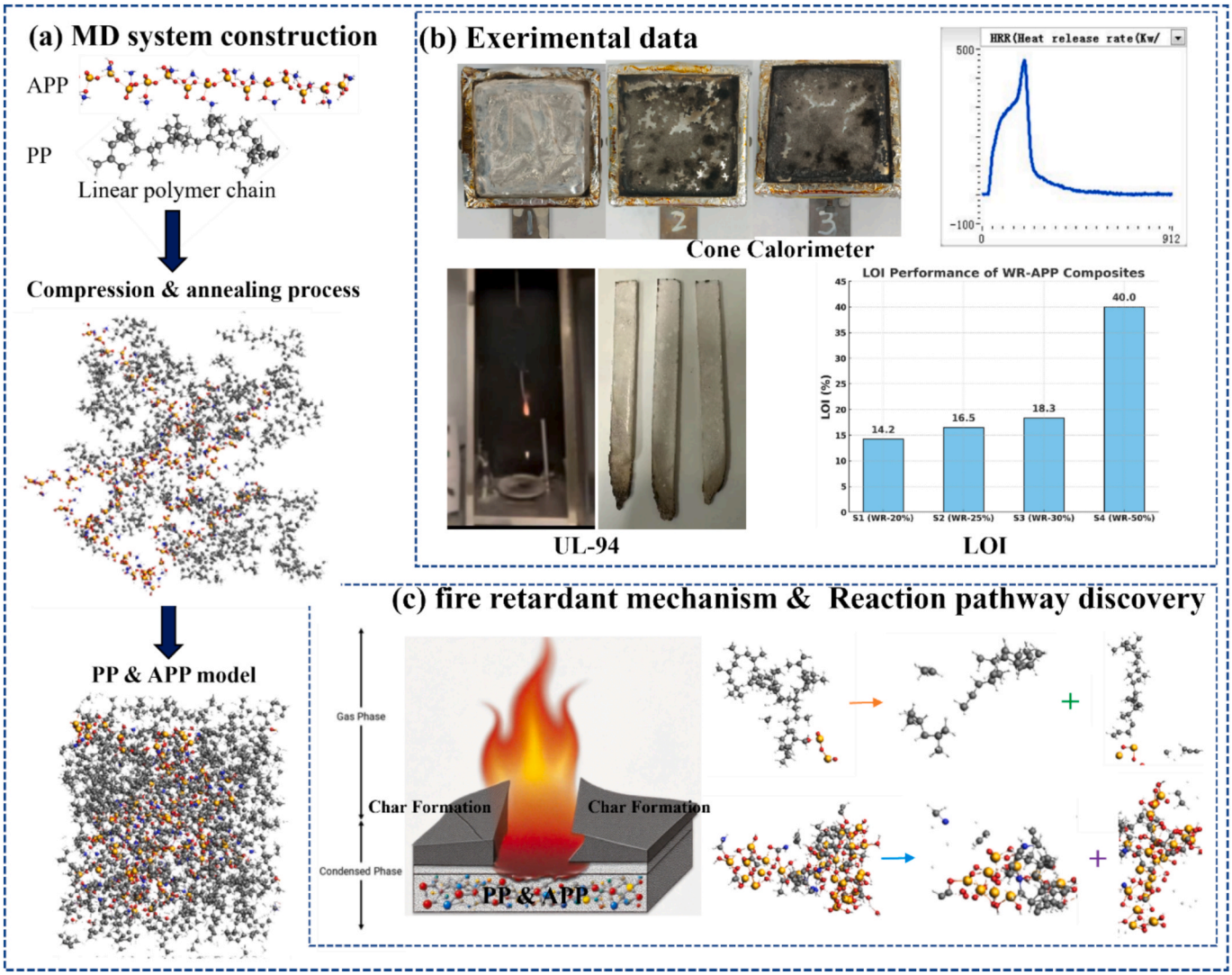

Fig. 1. Integrated research framework: (a) schematic of model implementation of MD system, (b) experimental fire performance evaluation, (c) fire retardancy mechanism characterisation through ReaxFF-MD.

still scarce.

To address these gaps, we combine ReaxFF-MD simulations with targeted fire-performance experiments to clarify the thermal degradation mechanisms and fire behaviour of PP/APP composites. As schematically summarised in Fig. 1, the workflow involves three stages: (a) atomistic modelling of PP and APP followed by high-temperature ReaxFF-MD simulations to analyse key degradation pathways, char precursors and associated kinetic parameters; (b) systematic fire testing by cone calorimetry (HRR, THR, MLR, TSP, SEA and residue analysis), LOI and UL-94 vertical burning, complemented by evolved-gas analysis (TG-FTIR), unburned-composite dispersion characterisation (SEM), mechanical property evaluation, and residue morphology/composition characterisation (with 50 wt% residues provided in the Supporting Information); and (c) integration of the experimental and MD results into a consistent mechanistic picture that links acid-catalysed charring in the condensed phase with radical scavenging in the gas phase. Taken together, the study illustrates how molecular-scale ReaxFF-MD simulations can be coupled with standard fire tests to rationalise the structure–property relationships of APP in PP, and provides guidance for optimising halogen-free flame-retardant polyolefins.

2. Experimental

2.1. Materials and sample preparation

PP powder (150 mesh) was supplied by Guangdong Hengfa Plastics Co., Ltd. Two grades of ammonium polyphosphate (APP) with distinct polymerisation degrees and water solubilities were provided by Hong Kong Advanced Scientific Technology Limited. According to the supplier specifications, the low-polymerisation APP (denoted as WP-APP) has a degree of polymerisation < 20 and high solubility (>900 g/L at 25 °C), while high-polymerisation APP (denoted as WR-APP) possesses a polymerisation degree of 30–50 and low solubility (<4 g/L at 25 °C). PP/APP composites were fabricated by melt blending PP with APP at loadings of 20, 25, 30, and 50 wt% using a torque rheometer. The blends were subsequently hot-pressed to obtain sheets, from which test specimens were cut. The formulations are summarised in Table 1.

2.2. Characterisation methods

The flame retardancy of the composites was evaluated by the UL-94 vertical burning test (IEC 60695–11-10) and limiting oxygen index (LOI) measurement (ASTM D2863), using specimens of $130 \times 13 \times 3$ mm^3 and $100 \times 6.5 \times 3$ mm^3, respectively. Fire behaviour was further assessed by cone calorimetry (ISO 5660-1) at an external heat flux of 35 kW/m^2, providing heat release (HRR, THR), mass loss (MLR), smoke metrics (TSP, SEA) and oxygen-consumption parameters. To evaluate APP dispersion and interfacial features in the unburned composites, cryo-fractured surfaces were examined by SEM (JEOL JSM-7100F), and multi-field image analysis was used to semi-quantify particle distribution and agglomeration. Thermal decomposition and evolved volatiles were analysed by TG-FTIR: ~10.0 mg of sample was heated from 25 to 800 °C at 10 °C/min under N_2 (60 mL/min). Cone-calorimetry residues were characterised by SEM (JEOL JSM-7100F), XPS (PHI 5000 VersaProbe; C1s = 284.8 eV) and Raman spectroscopy (LabRAM HR Evolution, 532 nm). Representative formulations (WP-30, WR-20 and WR-30) were selected for direct comparison with the ReaxFF-MD simulations; residue data for the 50 wt% formulations are provided in the Supporting Information as a high-loading reference. Tensile tests were conducted on an Instron 5566 universal testing machine (±500 N), following ASTM D882-12 at a crosshead speed of 5 mm/min (n = 3), and results are reported as mean ± standard deviation.

Table 1
Formulation of PP/APP composites.

Sample ID	Flame retardant type	APP content (wt%)
PP	Neat PP	0
WP-20	WP-APP (soluble)	20
WP-25	WP-APP (soluble)	25
WP-30	WP-APP (soluble)	30
WP-50	WP-APP (soluble)	50
WR-20	WR-APP (insoluble)	20
WR-25	WR-APP (insoluble)	25
WR-30	WR-APP (insoluble)	30
WR-50	WR-APP (insoluble)	50

3. Mathematical models

3.1. Experimental formulae

To facilitate a quantitative comparison of combustion behaviour and smoke generation among the PP/APP formulations, two derived parameters were calculated from the cone calorimeter data: the average rate of heat emission (ARHE) and the smoke production rate (SPR).

The ARHE over a time interval $[t_1, t_2]$ was defined as **Eq. (1):**

$$\mathrm{ARHE} = \frac{1}{\Delta t}\int_{t_1}^{t_2} \mathrm{Q(t)dt} \tag{1}$$

where Q(t) is the instantaneous heat release rate and $\Delta t = t_2 - t_1$ is the duration of the interval.

The SPR describes the rate of smoke generation and was obtained from the slope of the total smoke production (TSP)–time curve as **Eq. (2):**

$$\mathrm{SPR} = \frac{\Delta \mathrm{TSP}}{\Delta t} \tag{2}$$

where ΔTSP is the change in total smoke production, and Δt is the time interval over which the change in TSP is observed. To ensure the accuracy of SPR, the TSP data is often smoothed to eliminate noise from experimental fluctuations.

3.2. ReaxFF model equations

ReaxFF is a reactive bond-order force field that allows bond breaking and formation during MD simulations. Detailed formulations are available in the original ReaxFF literature and are not repeated here.[41,42].

3.3. Model implementation

All simulations were equilibrated at 300 K for 50 ps to relax the initial configurations. The systems were then linearly heated from 300 K to the target pyrolysis temperatures (2500, 3000, and 3500 K) within 50 ps. After reaching the desired temperature, isothermal heating conditions were applied for additional 400 ps, resulting in a total simulation time of 500 ps for each case. Temperature control was achieved using a Nosé–Hoover thermostat with a damping constant of 50 fs, and the integration time step was fixed at 0.1 fs.

Atomistic models of PP/APP composites were constructed with systematically varied compositions and APP chain lengths. Two APP loadings (20 and 30 wt%) and two polymerisation degrees (n = 15 and n = 30) were considered, with a total of 12 distinct PP/APP molecular geometries. Detailed modelling parameters are provided in Table 2. Each simulation cell contained 20–30 isotactic PP chains with 20 repeat units each and 2–5 APP chains depending on the target composition. The initial configurations were generated at low packing density and then compacted to a target density of ~ 0.90 g/cm^3 to mimic experimental PP/APP blends, and a three-dimensional periodic boundary condition was applied. Atomic packing was generated using Packmol [43] and subsequently relaxed by energy minimisation. Taking the example of n = 30 with 30% APP loading, Fig. 2 illustrates the modelling process. The simulation system consists of 3 long APP chains and 24 PP chains,

Table 2
Modelling Details for PP/APP Composites.

Model No.	APP Polymerisation Degree (n)	APP Loading (wt%)	Temperature (K)	Density (g/cm^3)	Number of Atoms
1	15	19.98	2500	0.8926	5648
2		30.40		0.9329	5196
3		19.98	3000	0.8926	5648
4		30.40		0.9329	5196
5		19.98	3500	0.8926	5648
6		30.40		0.9329	5196
7	30	20.65	2500	0.9124	5458
8		30.40		0.9246	5184
9		20.65	3000	0.9124	5458
10		30.40		0.9246	5184
11		20.65	3500	0.9124	5458
12		30.40		0.9246	5184

totalling 5184 atoms. At the initial simulation time (0 ps), the system dimensions were 80 Å × 80 Å × 80 Å, and the density was 0.0934 g/cm^3. After 25 ps, the system dimensions reduced to 57 Å × 57 Å × 56 Å, with the density increasing to 0.2644 g/cm^3. By 50 ps, the system dimensions further decreased to 38 Å × 37 Å × 37 Å, and the density reached 0.9246 g/cm^3. The simulation was conducted with a time step of 0.25 fs, with a total of 200,000 steps, corresponding to the 50 ps compaction stage.. The ReaxFF force field for CHONP elements was adopted, which has been widely validated for polymer combustion and phosphorus-based flame retardants[38,44–46]. The use of elevated temperatures is a common acceleration strategy in ReaxFF-MD, enabling observation of thermal degradation within computationally feasible sub-nanosecond timescales [47]. The simulation data were post-processed using ChemTraYzer 2[48]. Note that ReaxFF-MD employs elevated temperatures and a finite periodic simulation cell to access reactive events within feasible time scales. Therefore, the simulation outputs are interpreted in terms of relative pathways and comparative trends rather than absolute kinetics at real fire temperatures; the growth/retention of heavy clusters (e.g., C40 + fraction) is used as a molecular-scale proxy for condensed-phase stabilisation and char-precursor formation, rather than a direct prediction of macroscopic char morphology or phase separation.

4. Results and discussion

4.1. Vertical burning test (UL-94)

The UL-94 vertical burning test was used to assess the anti-dripping behaviour and self-extinguishing ability of the PP/APP composites. UL-94 explicitly accounts for melt dripping and secondary ignition via the cotton-ignition criterion, providing a dripping-tolerant complement to LOI.As summarised in Table 3, neat PP shows long afterflame times (T_1 ≈ 35 s) with heavy flaming dripping and receives no UL-94 rating. For WR-APP, increasing loading leads to a clear improvement. At 20 and 25 wt%, T_1/T_2 are reduced to 9 ± 5/14 ± 3 s and 6 ± 2/9 ± 2 s, but flaming drips still ignite the cotton (V-2). At 30 wt%, T_1/T_2 decrease to 2.5 ± 1/3 ± 2 s, dripping is very limited and cotton ignition is largely suppressed (V-1). At 50 wt%, the samples self-extinguish rapidly (0.5 ± 0.5/1 ± 0.5 s) without dripping or cotton ignition, achieving V-0. For WP-APP, At 20 and 25 wt%loadings, T_1 (74 ± 3 s and 89 ± 6 s) is even longer than for neat PP, and heavy flaming dripping ignites the cotton (no rating). An improvement appears at 30 wt% (24 ± 12/15 ± 5 s, V-2), and 50 wt% is required to reach V-0 (2.6 ± 1/3 ± 2 s) with no or only slight dripping

Table 3
UL-94 vertical burning test results of pristine PP and PP/APP composites.

Sample	T1 (s)	T2 (s)	Dripping	Cotton ignition	UL-94 rating
PP	34.5 ± 22	–	Heavy	Yes	No rating
WR-20%	9 ± 5	14 ± 3	Light	Yes	V-2
WR-25%	6 ± 2	9 ± 2	Light	Yes	V-2
WR-30%	2.5 ± 1	3 ± 2	Very light	No/Partial	V-1
WR-50%	0.5 ± 0.5	1 ± 0.5	No	No	V-0
WP-20%	74 ± 3	–	Heavy	Yes	No rating
WP-25%	89 ± 6	–	Heavy	Yes	No rating
WP-30%	24 ± 12	15 ± 5	Light	Yes	V-2
WP-50%	2.6 ± 1	3 ± 2	No / Very light	No	V-0

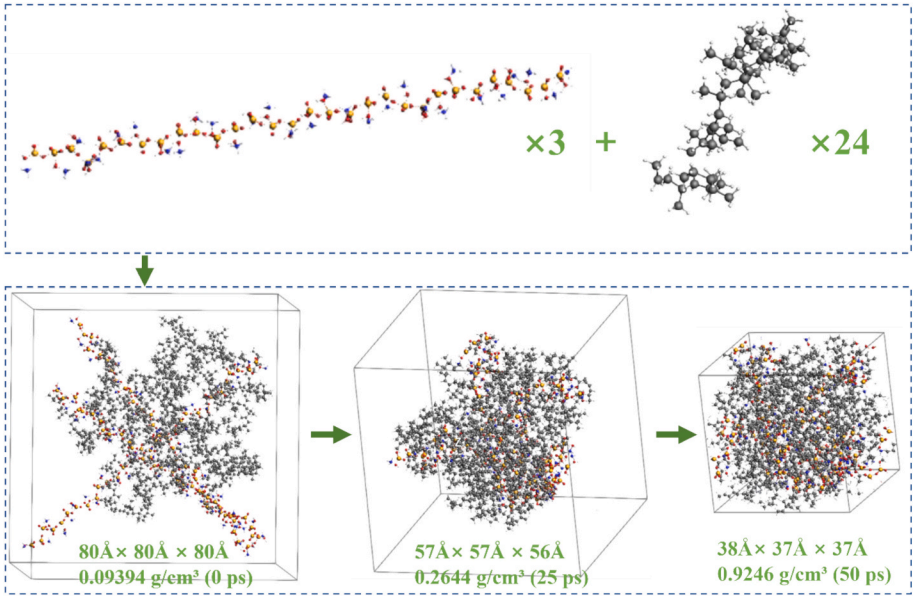

Fig. 2. Modelling Details for PP/APP Composite with 30n, 30% APP Loading.

and no cotton ignition. Thus, WR-APP reaches self-extinguishing, non-dripping behaviour at lower loading than WP-APP, and WR-30 outperforms WP-30 at the same 30 wt% loading.

4.2. Limited oxygen Index(LOI)

The LOI test was used to further characterise the flammability of the PP/APP composites. For neat PP and all PP/WP-APP formulations, stable burning in the LOI apparatus could not be maintained under ASTM D2863 conditions: the specimens melted and dripped out of the flame zone, so no reliable LOI values could be determined. This behaviour is consistent with the severe melt-dripping observed in the UL-94 tests. In contrast, PP/WR-APP composites exhibit measurable and progressively increasing LOI values with increasing WR-APP loading. As shown in Fig. 3, the LOI increases from 14.2% for WR-20 to 16.5% for WR-25 and 18.3% for WR-30, and reaches about 40.0% for WR-50, at which point the specimens show stable self-extinguishing without dripping. The monotonic increase in LOI with WR-APP content indicates that WR-APP improves the resistance of PP to ignition and sustained flaming in oxygen-enriched atmospheres. Taken together with the UL-94 results, the LOI data suggest that, under the present test conditions, WR-APP is more effective than WP-APP in reducing flammability and suppressing melt-dripping, particularly at high loadings where self-extinguishing, non-dripping behaviour is obtained. In the following sections, these contrasting behaviours are discussed in relation to differences in char structure and to the polymerisation degree and water solubility of the two APP grades.

4.3. Cone calorimeter analysis

Cone calorimetry was used to quantify the heat release, mass loss and smoke production behaviour of the PP/APP composites. As shown in Fig. 4a, neat PP exhibits a single sharp HRR peak at around 200 s (pHRR $\approx$ 650 kW/m^2) followed by a rapid decay, indicating a short but intense burning period. After APP is added, the HRR peaks of all composites are lower than that of neat PP and the curves become broader. With increasing WR-APP or WP-APP loading, the HRR peak values show an overall decreasing trend, with WR-30, WR-50 and WP-50 giving the lowest peaks, which indicates that APP addition suppresses the instantaneous heat release during the main burning stage. Fig. 4b shows that neat PP has the highest final THR, whereas all PP/APP composites exhibit lower THR curves that level off to a plateau, demonstrating a reduction in total heat release; for each APP type, higher loadings lead to lower final THR.Fig. 4c presents the bar charts of the maximum mass loss rate (Max-MLR) and average mass loss rate (Avg-MLR). Neat PP has the highest Max-MLR. After APP incorporation, both Max-MLR and Avg-MLR decrease for all composites, and the formulations with higher WR-APP or WP-APP loadings exhibit relatively lower mass loss rates, indicating that the overall thermal degradation process is slowed. Fig. 4d summarises the smoke-related parameters (SEA and TSP) together with oxygen-consumption-related metrics. Neat PP shows relatively high SEA and TSP, whereas most APP-containing formulations display clear reductions. The oxygen-consumption-related parameter varies with formulation and reaches its minimum for WR-50, which is consistent with the reduced combustion intensity observed for the WR series. The fire hazard indices ARHE and SPR in Fig. 4e are consistent with these observations. Neat PP has the highest ARHE and SPR values, while both indices decrease upon APP addition. Among all formulations, WR-30 and WR-50 show the lowest SPR values. Under the present test conditions, the cone calorimeter results therefore show that APP incorporation reduces the peak and total heat release of PP, slows mass loss and decreases smoke generation. At medium and high loadings, the high-polymerisation WR-APP produces more pronounced reductions in HRR, MLR and smoke-related parameters than WP-APP, in line with the trends observed in the UL-94 and LOI tests, and providing experimental support for the mechanistic analysis based on ReaxFF-MD in the following sections.

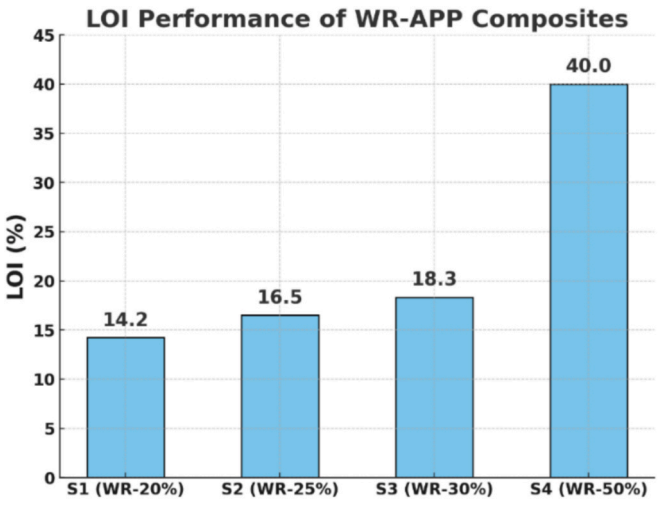

Fig. 3. LOI Performance of WR-APP Composites.

4.4. Tensile properties and modulus of PP/APP composites

Fig. 5 compares the tensile properties of the formulations (mean ± SD, n = 3); numerical values are summarised in Table S1 (Supporting Information). Compared with neat PP, incorporating APP leads to an overall increase in stiffness accompanied by reduced ductility: Young's modulus increases, whereas the tensile strain at maximum load (ε_max) decreases and the tensile stress at maximum load (σ_max) shows an overall downward trend. This behaviour is consistent with a typical particulate-filler effect: the rigid APP phase increases elastic constraint, while reduced deformability and stress transfer make tensile performance more sensitive to dispersion- and interface-related defects. At the same loading level, mechanical retention differs between the WP and WR systems. Overall, in the 20–30 wt% range, the WP series exhibits relatively higher ε_max and σ_max, whereas the WR series shows an earlier decrease in ductility and strength. The higher scatter for some WR formulations suggests a greater sensitivity of the macroscopic response to specimen-to-specimen heterogeneity. When the APP content increases to 50 wt%, both systems show further reductions in ε_max and σ_max, consistent with more pronounced embrittlement. This is consistent with increased particle–particle contact and local packing at high loadings, which intensifies the constraint imposed by interfacial discontinuities on load-bearing and deformation. Meanwhile, the modulus remains at a relatively high level, reflecting the sustained contribution of the rigid phase to composite stiffness. Tensile behaviour in particulate-filled systems is typically governed by dispersion uniformity, agglomerate size and interfacial debonding/pull-out. To support the above interpretation, Section 4.5 examines unburned-composite cross-sections by SEM and provides image-based agglomerate statistics for comparing APP distribution and agglomeration.

4.5. Morphology: Unburned composites and combustion residues

4.5.1. Unburned composite morphology and APP dispersion

At the 2 μm scale, two typical APP-related morphological features are observed in the unburned PP/APP composites (Fig. 6): (i) protrusions or local accumulations of particles/agglomerates on the fracture surface, and (ii) cavities/pits left by particle pull-out. These features reflect the spatial distribution of the filler in the matrix and local interfacial debonding/pull-out behaviour. As only limited fields of view are shown, the following comparison is qualitative. For the WR series, WR-20 is dominated by finely dispersed particles without obvious large-scale continuous accumulations; only a few small cavities/pits are

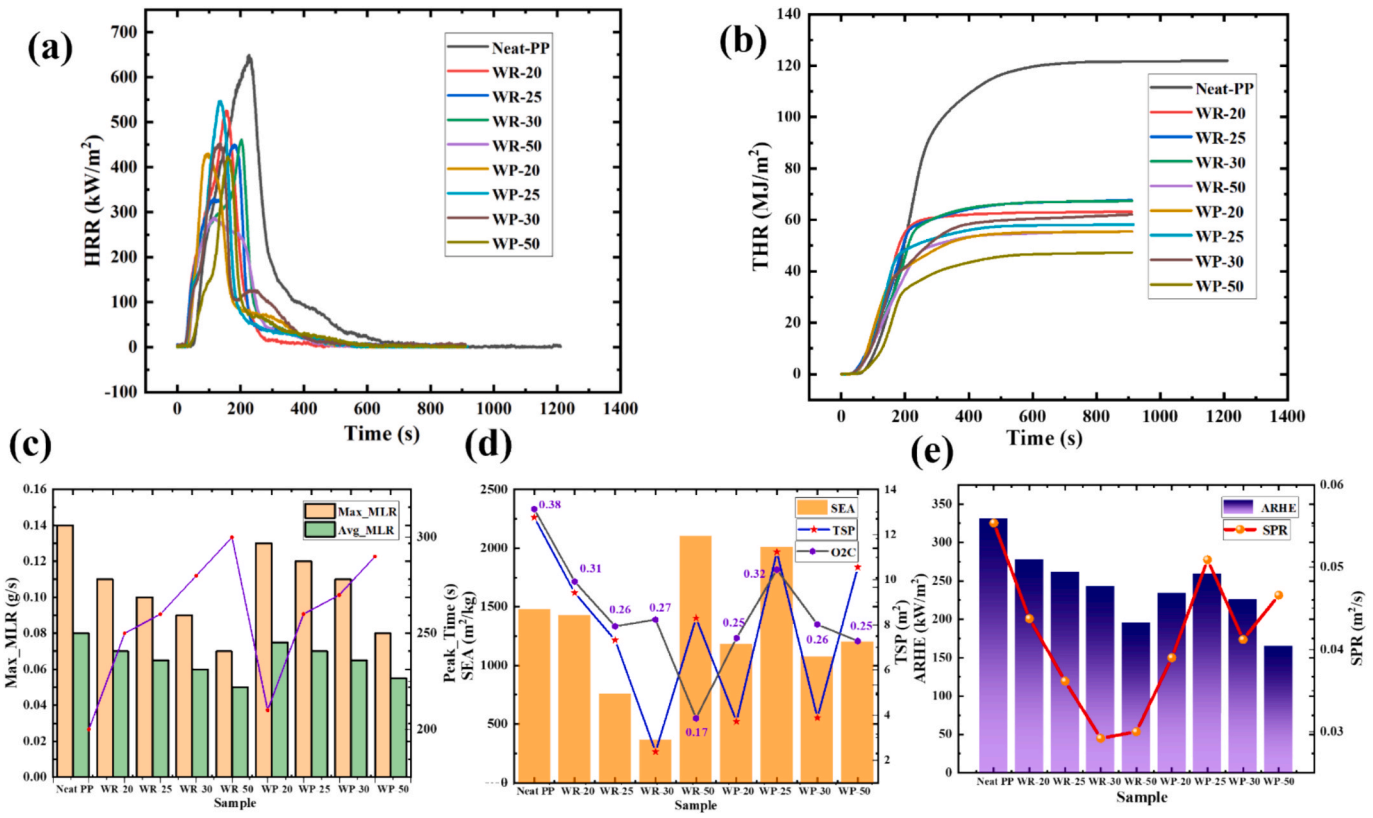

Fig. 4. Cone calorimeter results of PP/APP composites: (a) Heat release rate (HRR), (b) Total heat release (THR), (c) Mass loss rate (MLR), (d) Smoke and toxic gas parameters (SEA, TSP, O_2C), and (e) Average rate of heat emission (ARHE) with SPR.

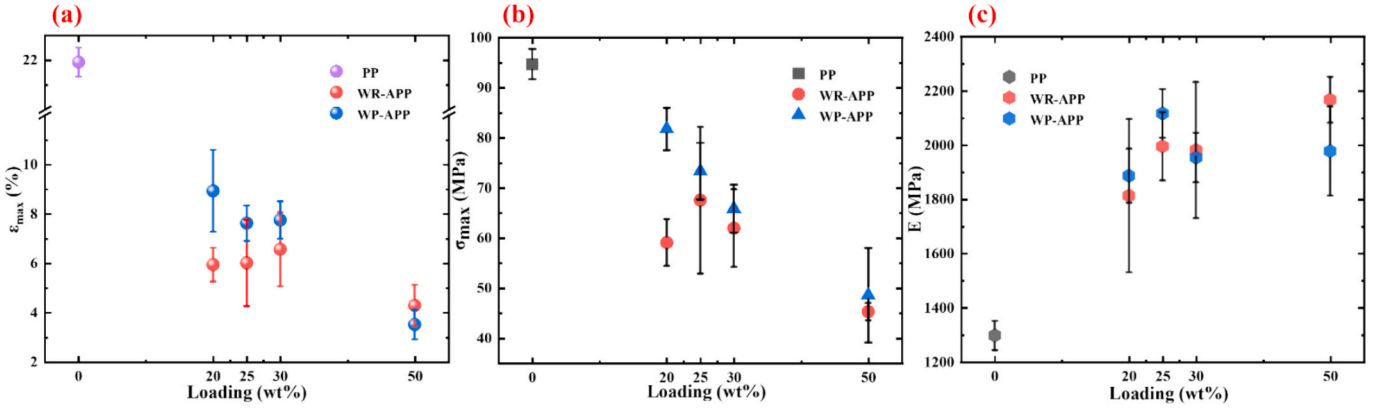

Fig. 5. Tensile properties of PP/APP composites versus APP loading (mean ± SD, n = 3): (a) tensile strain at maximum load, ε_max; (b) tensile stress at maximum load, σ_max; (c) Young's modulus, E.

locally observed, indicating occasional particle pull-out while the overall distribution remains relatively dispersed. At 30 wt% (WR-30), the particle density increases and pull-out pits/notches become more apparent, together with locally larger particles or agglomerates. For WR-50, larger cavities/collapsed regions and interfacial damage are observed, accompanied by local particle clustering, suggesting increased morphological non-uniformity at high filler loading. For the WP series, WP-20 appears relatively dispersed in some fields of view, but larger near-spherical agglomerates are also observed, indicating that local coarse agglomeration can occur even at low loading. The contrast between different fields of view is more pronounced for WP-30: some regions contain fewer particles and a relatively smooth matrix surface, whereas others show larger irregular agglomerates with cracks, consistent with non-uniform distribution and local enrichment. For WP-50, one field of view exhibits numerous round cavities/pits, while another shows increased particle accumulation with a broader particle-size distribution, indicating more pronounced local stacking at high loading. As the APP loading increases from 20 to 50 wt%, both series show a higher particle population and a greater tendency for local enrichment and interfacial defects. This morphological heterogeneity is consistent with the decreases in ε_max and σ_max and the increased scatter observed in tensile testing (Section 4.4), suggesting that agglomeration and interfacial discontinuities are more likely to act as failure initiation sites at high loadings. The implications of these features for residue/char formation are discussed in the following sections.

4.5.2. *Residue morphology and structure*

Fig. 7a shows the macroscopic residues of selected PP/APP

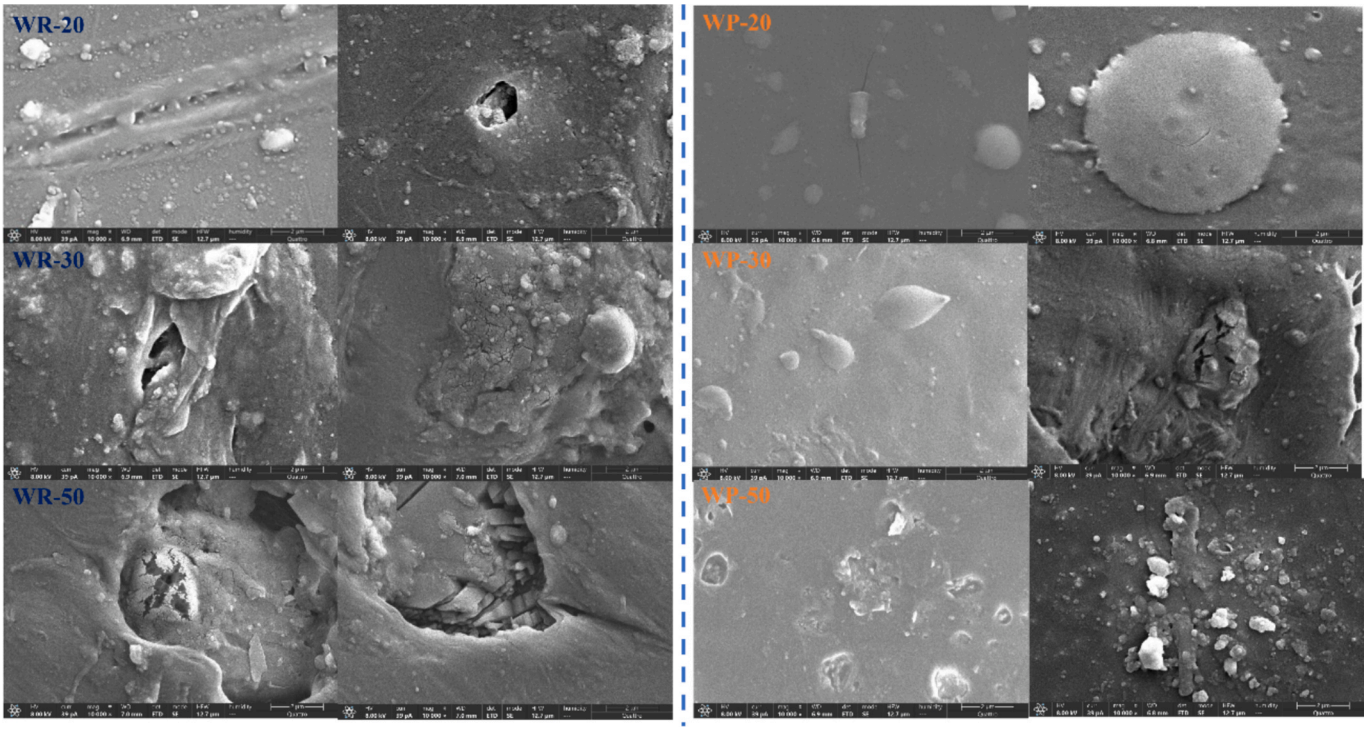

Fig. 6. SEM micrographs of unburned PP/APP composites showing APP dispersion (WR vs WP at 20, 30 and 50 wt%; scale bar: 2 μm).

composites after cone calorimetry (neat PP, WR-20, WR-30, WP-20 and WP-30). Neat PP is almost completely consumed and does not form a clear intumescent char layer. In contrast, all APP-containing samples retain an expanded, dark surface layer. For WR-20, the char does not fully cover the specimen and exposed regions are still visible, whereas WR-30 shows more uniform dark coverage with fewer gaps. Both WP-20 and WP-30 form macroscopic char layers that cover most of the surface; the char of WP-30 appears relatively more uniform and continuous, while WP-20 shows some variation in texture. To relate the structural features of APP (polymerisation degree and loading) to condensed-phase behaviour and to compare with the ReaxFF-MD simulations, three representative formulations—WR-20, WR-30 and WP-30—were selected for detailed microstructural analysis. Given the mechanical/dispersion constraints at 50 wt%, we focus on 20–30 wt% formulations aligned with ReaxFF-MD; 50 wt% macroscopic residues are provided in Fig. S1. Fig. 7b presents SEM images of these three residues at 5,000 × and 20,000 × magnifications. At lower magnification, the char of WR-20 shows particle agglomeration with visible cracks, indicating that the layer is not fully continuous at this loading. WR-30 exhibits a more strongly expanded, honeycomb-like morphology with finer features, suggesting a more developed intumescent structure, although local voids are still present. The surface of WP-30 is relatively compact, with fewer large cavities, but shrinkage cracks and pores can be observed. At higher magnification, WR-20 consists of discrete particles and island-like domains separated by fissures; WR-30 shows a network of closely packed, foam-like structural units; and WP-30 presents a relatively fused carbon matrix containing embedded pores and cracks. These morphological differences suggest that the two APP types may promote char expansion and densification in different ways. The elemental composition and distribution of the residues were examined by EDS (Fig. 7c). The spectra confirm the presence of C, O, P and N in all three chars, consistent with APP-derived retention in the condensed phase. Elemental mapping indicates that P- and N-containing signals are distributed across the char surface with local enrichment in specific regions (representative maps are shown in Fig. 7c(ii)–(iii)). Overall, WR-30 shows an expanded cellular char and stronger P/N signals than WP-30, while WP-30 exhibits a denser surface with shrinkage cracks at the same loading.

To evaluate the structural ordering of the condensed-phase char, Raman spectroscopy was carried out on WR-20, WR-30 and WP-30, with ten randomly selected spots measured for each sample (Fig. 8a). All spectra show the two characteristic bands of carbonaceous char: the D band (≈1350 cm^{-1}), associated with structural defects and disordered carbon, and the G band (≈1580 cm^{-1}), arising from graphitic sp^2 carbon. The I_D/I_G ratio was used as a comparative indicator of defect density/structural disorder in the char. For WR-20, the D and G bands are relatively broad and the average I_D/I_G is 1.23 ± 0.02, consistent with a largely disordered char. WR-30 exhibits a somewhat sharper G band, a weaker D band and a lower I_D/I_G of 0.87 ± 0.01, indicating a higher structural ordering. WP-30 has the highest I_D/I_G value (1.34 ± 0.02), which is consistent with the more fragmented char morphology observed by SEM.

To probe the chemical environments in the residues, high-resolution XPS analysis was conducted (Fig. 8b). Raman and XPS results for the 50 wt% formulations are provided in **Fig. S2** (Supporting Information).The C 1 s spectra of all three samples can be deconvoluted into components at about 284.8 eV (C–C), ~286.0 eV (C–N/C–O/C–P) and ~ 287.8 eV (C=N/C=O), indicating the coexistence of graphitic carbon and heteroatom-containing carbon species in the char. The N 1 s spectra for each sample contain two main peaks, assigned to C–N (≈398.3 eV) and C=N (≈400.0 eV), in agreement with Marton et al.[49]. N-related signals are stronger for WR-20 and WR-30 than for WP-30, suggesting differences in nitrogen retention.The P 2p spectra exhibit a doublet assigned to P–C $2p_{3/2}$ and $2p_{1/2}$ at binding energies of about 133.5 and 134.5 eV, respectively, consistent with P–C environments reported by Sun et al.[50]. The presence of this doublet in all three samples indicates that part of the phosphorus remains chemically bound in the char matrix rather than being completely volatilised during burning. Overall, the Raman and XPS results indicate that WR-30 forms a more ordered carbon structure with stronger N/P signals, whereas the residues of WR-20 and WP-30 are less graphitised and more defective, consistent with the SEM/EDS observations. Because polymerisation degree, surface state and particle characteristics are coupled with the apparent water solubility of the two commercial APP grades, the discussion above is

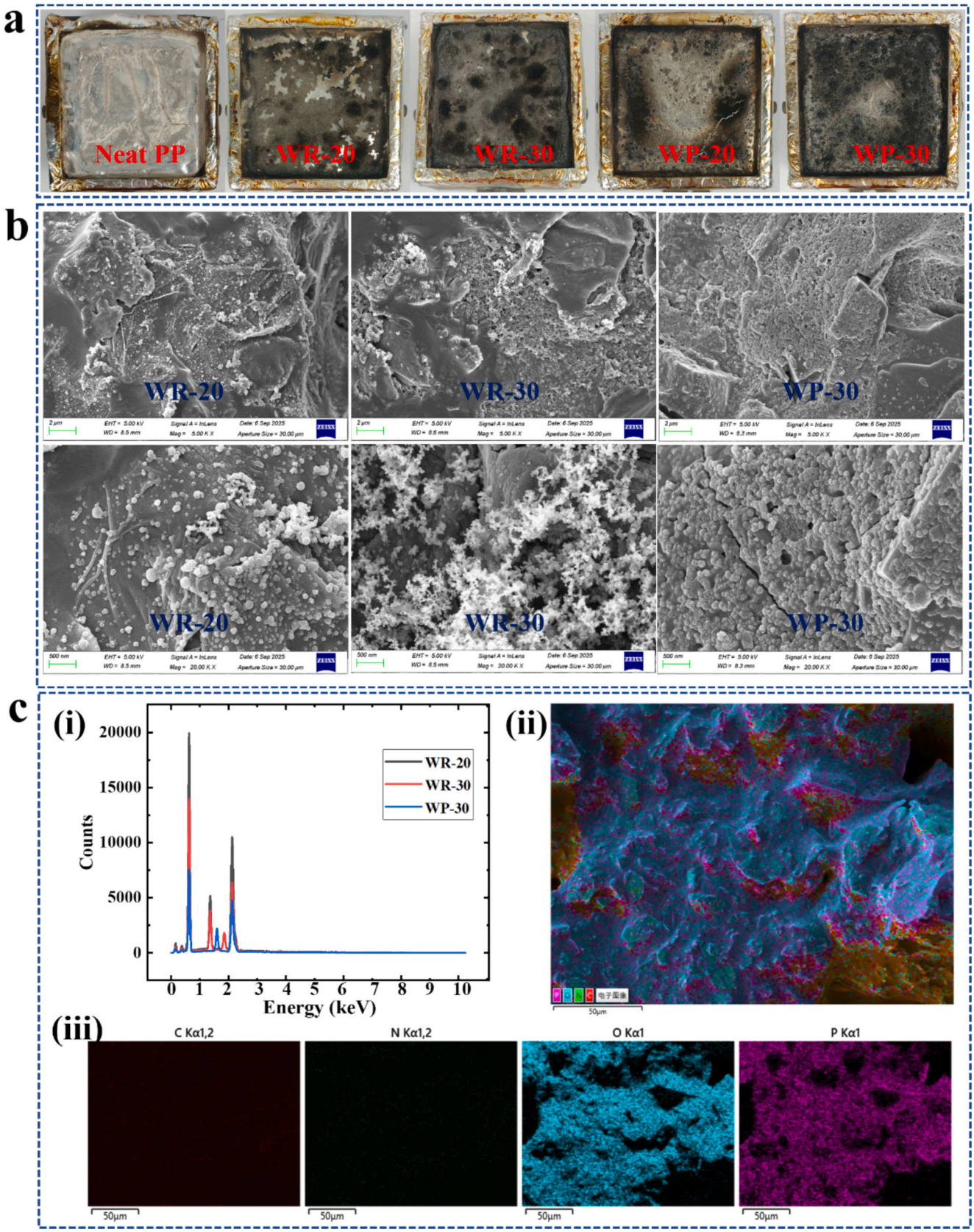

Fig. 7. Morphology of residual carbon layer: a image of combustion residue, b SEM morphology (low magnification above, high magnification below), c EDS Mapping (i) total spectrum comparison; (ii) Layered EDS Mapping (iii) Elemental distribution map of C, N, O, P elements in the carbon seam of WR-30 sample (corresponding to C Kα1,2, N Kα1,2, O Kα1, P Kα1).

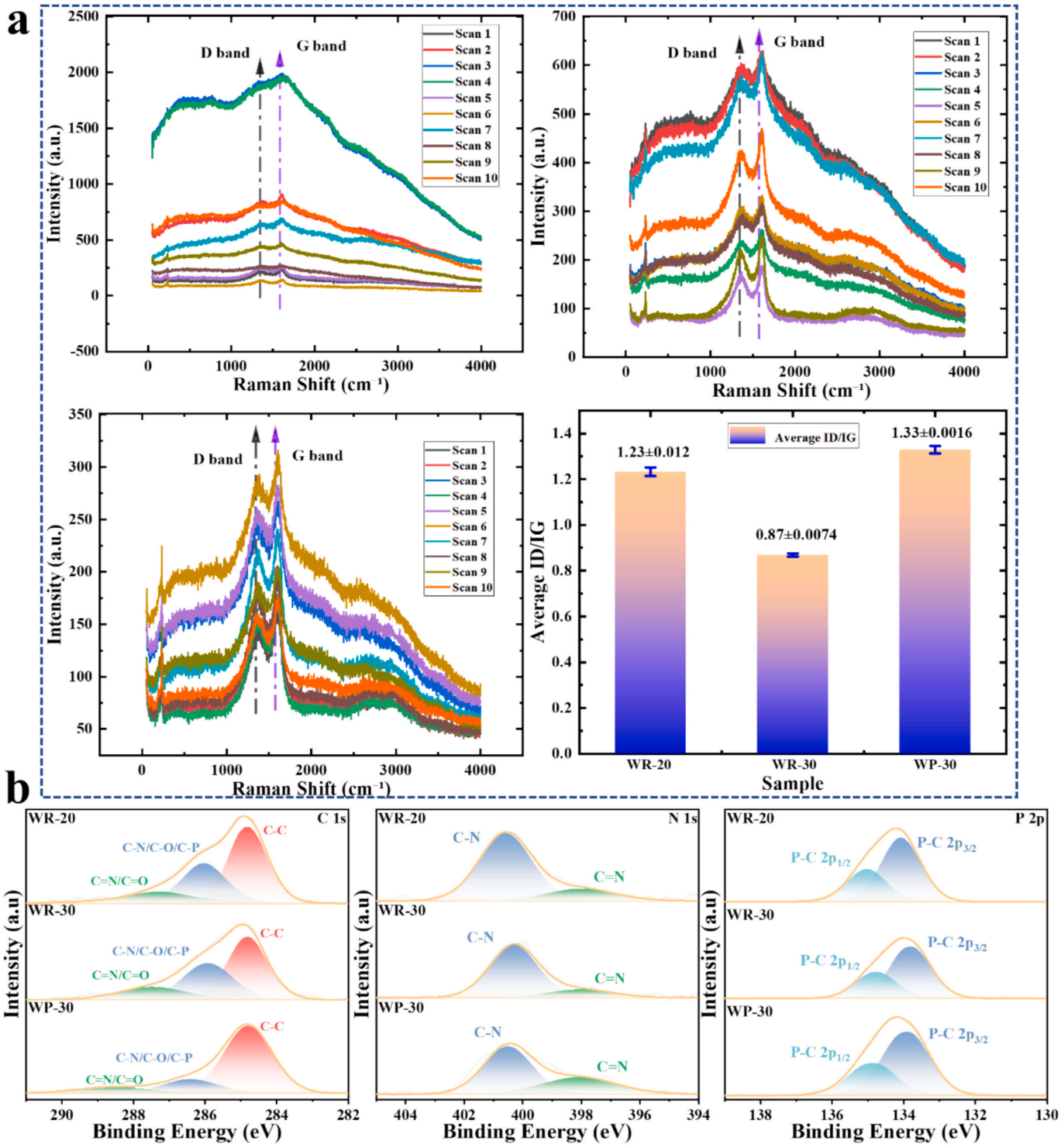

Fig. 8. Composition characterisation of residual carbon: a Raman spectra; b XPS spectra.

intended to explain the relative differences between WP-APP and WR-APP under identical processing conditions, rather than to decouple water solubility as an independent variable.

4.6. TG–FTIR analysis of evolved gases

Fig. 9 compiles the TG–FTIR 3D spectra of WP-30 and WR-30 together with the temperature-resolved FTIR spectra, illustrating the evolution of pyrolysis volatiles with temperature. Under identical test conditions, both systems show comparable characteristic bands: a pronounced CO_{22} absorption at ≈2350 cm^{-1}, aliphatic C–H stretching in the 3000–2800 cm^{-1} region (hydrocarbon fragments), bands in the ≈1600–1450 cm^{-1} region associated with unsaturated C=H-related species, and an NH_3-related region near ≈1000 cm^{-1}. These bands intensify within the main pyrolysis temperature window and exhibit consistent peak positions in the extracted spectra, indicating broadly similar volatile "fingerprints" for the two formulations. The main differences lie in the temperature distribution and relative intensity of these bands. As indicated by the relative absorbance profiles, WR-30 shows a more concentrated CO_2 signal during the main pyrolysis

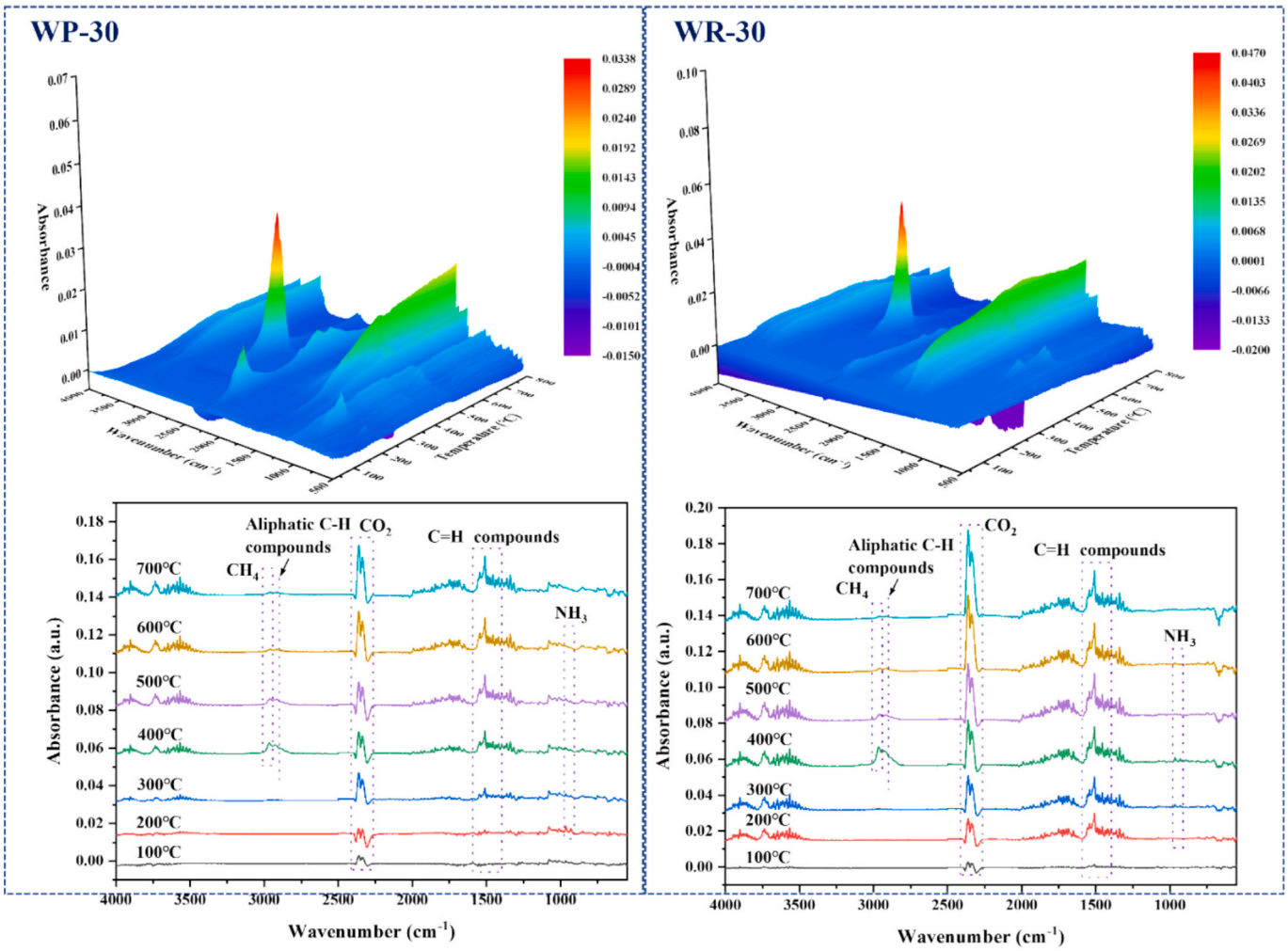

Fig. 9. TG–FTIR analysis of evolved volatiles from WP-30 and WR-30: 3D FTIR maps and temperature-resolved spectra.

stage, whereas the hydrocarbon-related bands in WP-30 (C–H and C=H regions) extend over a wider temperature range and persist for longer. These observations are qualitatively consistent with the fire-performance trends and support the subsequent ReaxFF-MD discussion by providing an experimental reference for differences in hydrocarbon evolution and the associated condensed-phase development.

4.7. ReaxFF-MD simulation results

Note that the ReaxFF-MD simulations were performed at accelerated temperatures (2500–3500 K) to access degradation events within sub-nanosecond timescales; therefore, the results are interpreted comparatively to reveal relative trends and pathways rather than to predict kinetics at real pyrolysis temperatures.

4.7.1. Gas-phase hydrocarbons

Fig. 10(a) shows the temporal evolution of the main hydrocarbon products. Under the accelerated ReaxFF-MD conditions, C_2H_4 and CH_4 are the dominant volatile hydrocarbons, whereas C_3H_6 remains a minor product. Increasing temperature from 2500 to 3500 K shifts hydrocarbon formation to earlier times and increases the overall product levels, indicating faster degradation at higher temperature. At 2500–3000 K, the presence of APP generally reduces and/or delays hydrocarbon formation relative to the corresponding PP-rich systems, and the effect is more evident at higher APP loading and higher polymerisation degree, particularly for CH_4. At 3500 K, the differences between formulations become much less distinct, consistent with rapid high-temperature fragmentation and secondary reactions. These comparative trends are consistent with the reduced heat/smoke release observed in cone calorimetry and with the delayed evolution of key volatiles observed in TG-FTIR.

4.7.2. Condensed-phase residue

In the simulations, the formation of heavy condensed-phase species was tracked using the C_{40+} carbon fraction, which is taken as an approximate indicator of char precursors (Fig. 10b). Overall, the C40 + fraction remains low (≈1.4–2.9%) across all cases, with only a moderate temperature dependence within 2500–3500 K. For n = 15, the 20 wt% APP systems yield C40 + fractions of 2.38–2.94% across the three temperatures, whereas the 30 wt% APP systems give 1.57–1.73%. A similar trend is observed for n = 30, where the 20 wt% APP systems give 2.23–2.83% and the 30 wt% APP systems give 1.41–1.69%. It should be noted that C40 + tracks carbon-rich clusters only and does not account for phosphorus-/oxygen-containing condensed-phase fragments; therefore, this metric is used here for comparative assessment of heavy-fragment formation in the MD simulations rather than as a direct predictor of experimental char yield. The experimental residue structure and heteroatom retention are discussed based on SEM/Raman/XPS in Section 4.5.2.

To elucidate the synergistic effects of APP content, polymerisation degree, and pyrolysis temperature on the thermal degradation of PP/APP composites, the mass loss and rate curves under different conditions were compared (Fig. 11**(a–d)**), the microscopic morphological evolution was analyzed by combining molecular dynamics snapshots (Fig. 12).

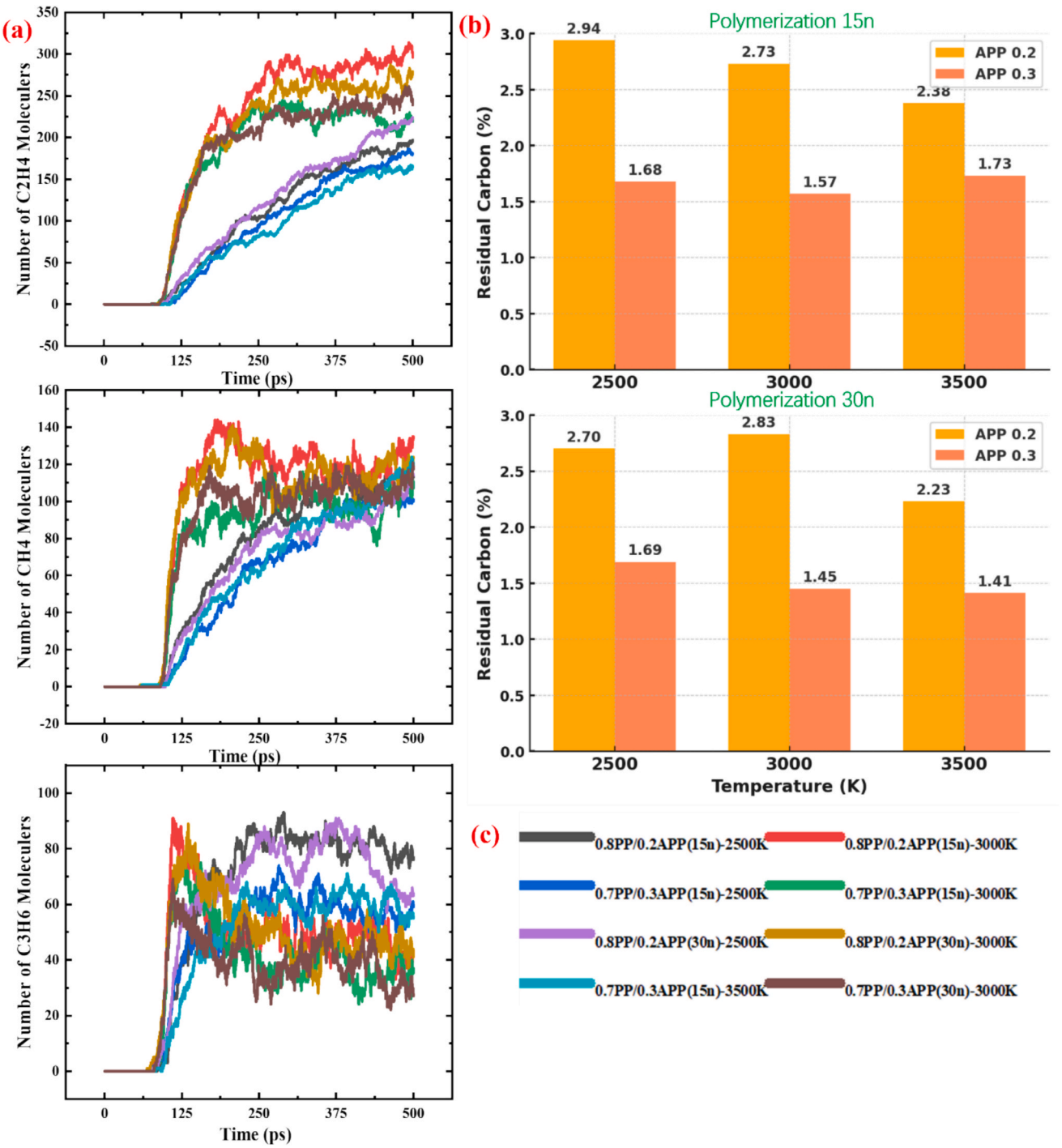

Fig. 10. Gas-phase hydrocarbon evolution and condensed-phase char formation:(a) evolution of major small hydrocarbons (C_2H_4, CH_4, C_3H_6); (b) residual carbon (C_{40+}) yield at different APP contents, polymerisation degrees, and temperatures; (c) legend corresponding to panel (a).

Products were classified into C#≤ 5 (small gaseous molecules), C# ≤ 20 (intermediate fragments), and C#≥40 (large clusters in the condensed phase). Four representative systems were analyzed: 0.3APP–15n–2500 K, 0.3APP–30n–2500 K, 0.2APP–30n–2500 K, and 0.3APP–30n–3000 K.

4.7.3. *Effect of polymerisation degree*

The influence of APP polymerisation degree can be seen by comparing the 0.3APP–15n–2500 K and 0.3APP–30n–2500 K systems (Fig. 11a,b). For small molecules (C#≤ 5), increasing n from 15 to 30 shifts the onset of release from 99.75 ps to 108.50 ps, and the t_{s0} values of the C_{20} and C_{40} fractions are also delayed by about 3–4 ps. In the main decomposition stage, the 30n system shows slightly higher but narrower peaks (for example, the peak rate of the C_{20} fraction is 0.4099 ps^{-1} vs 0.3948 ps^{-1}). Within the present simulation window, a higher APP polymerisation degree therefore leads to a limited but clearly observable delay in degradation.

4.7.4. *Effect of APP content*

At fixed polymerisation degree (30n) and temperature (2500 K), the effect of APP loading can be identified by comparing the 0.3APP and 0.2APP systems (Fig. 11b,c). When the APP content is reduced from 0.3 to 0.2, the onset of C# ≤ 5 release shifts earlier from 108.50 ps to 95.50

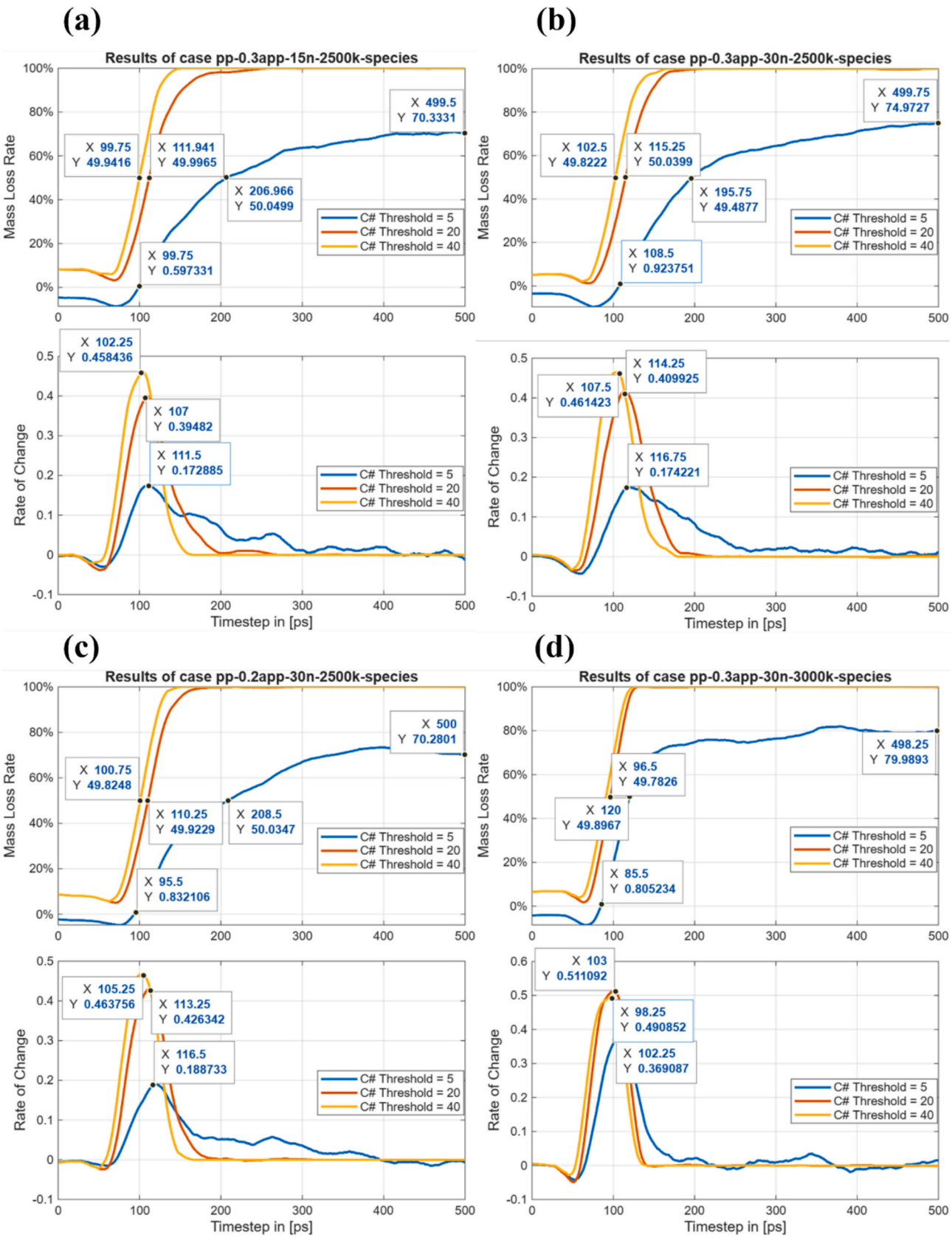

Fig. 11. Comparative pyrolysis behaviours of PP/APP composites under different conditions.

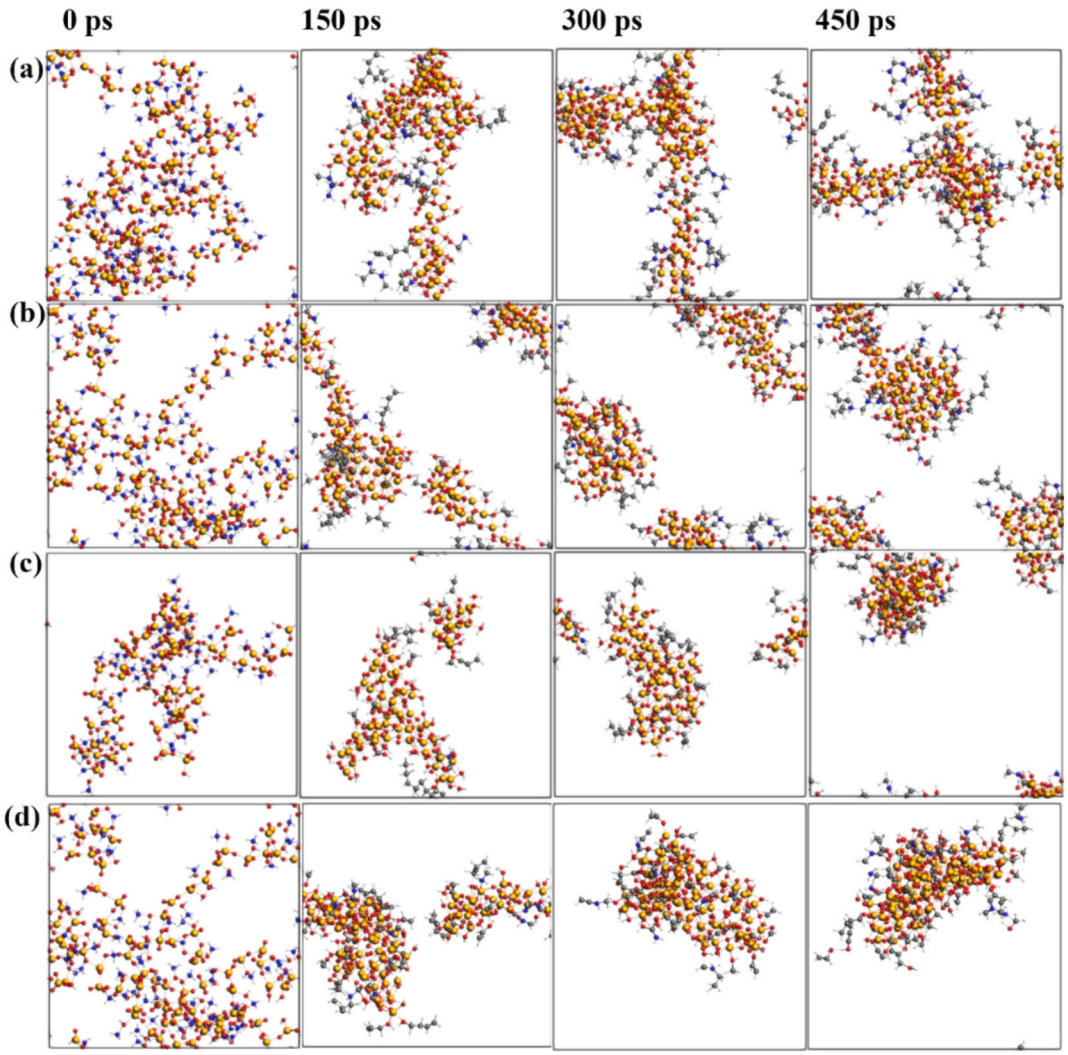

Fig. 12. Snapshots of polyphosphate chunks at 0/150/300/450 ps: (a) 0.3APP–15n–2500K, (b) 0.3APP–30n–2500K, (c) 0.2APP–30n–2500 K, and (d) 0.3APP–30n–3000 K.

ps, and the final fraction of small molecules decreases from 74.97% to 70.28%. The t_{s0} values of the C_{20} and C_{40} fractions are advanced to 110.25 ps and 100.75 ps, respectively. These features indicate that lowering the APP content weakens the delaying effect on pyrolysis.

4.7.5. *Effect of temperature*

Under the 0.3APP, 30n condition, the temperature effect can be assessed from Fig. 11b and Fig. 11d. Increasing the temperature from 2500 K to 3000 K markedly shortens the induction period: the onset of C# $\leq$ 5 release moves from 108.50 ps to 85.50 ps, and the final fraction of small molecules increases to 79.99%. The t_{s0} values of the C_{20} and C_{40} fractions are brought forward to 102.25 ps and 96.50 ps, and the corresponding peak rates also increase, for example from 0.4614 ps^{-1} to 0.5111 ps^{-1} for C_{40}. These changes show that higher temperature accelerates bond scission and fragment formation, and at the same time reduces the ability of the condensed phase to delay volatile release.

Taken together, at a given temperature, higher APP polymerisation degree and content are associated with a longer induction period and a more concentrated decomposition process, whereas increasing temperature shows the opposite trend. This “delay–acceleration” balance is qualitatively consistent with the cone calorimetry results, where formulations with suitable APP structure and loading exhibit lower heat release and more developed char layers.

4.7.6. *Morphology of APP-Rich polyphosphate clusters*

Fig. 12 shows representative MD snapshots of APP-rich regions for different APP loadings, polymerisation degrees and temperatures. At 2500 K, the system with higher polymerisation degree (30n) and higher APP content (0.3) forms larger and more connected polyphosphate clusters, whereas lower APP content (0.2) or lower polymerisation degree (15n) mainly yields smaller, more separated aggregates. At 3000 K, the clusters in the 0.3APP–30n system become more irregular and porous than at 2500 K. These qualitative trends are consistent with the kinetic differences discussed in Section 4.5.3–4.5.5.

4.7.7. *Gas-phase product and radical distributions*

Fig. 13 summarises the effects of temperature, APP content and polymerisation degree on the distributions of major small molecules and some heteroatom-containing species. At fixed APP content (0.3) and polymerisation degree (30n), temperature has the strongest influence (top panel). The mole fraction of C_2H_4 increases from about 13% at 2500 K to about 23% at 3000 K. CH_4 also increases with temperature. The fractions of some oxygen-containing products (e.g. HO and H_2O) are slightly higher at 2500 K than at 3000 and 3500 K. Overall, increasing temperature shifts the product spectrum toward lighter hydrocarbons and increases the relative abundance of the dominant gaseous species. At 2500 K and polymerisation degree 15n (middle panel), increasing the APP content from 0.2 to 0.3 leads to small but systematic decreases

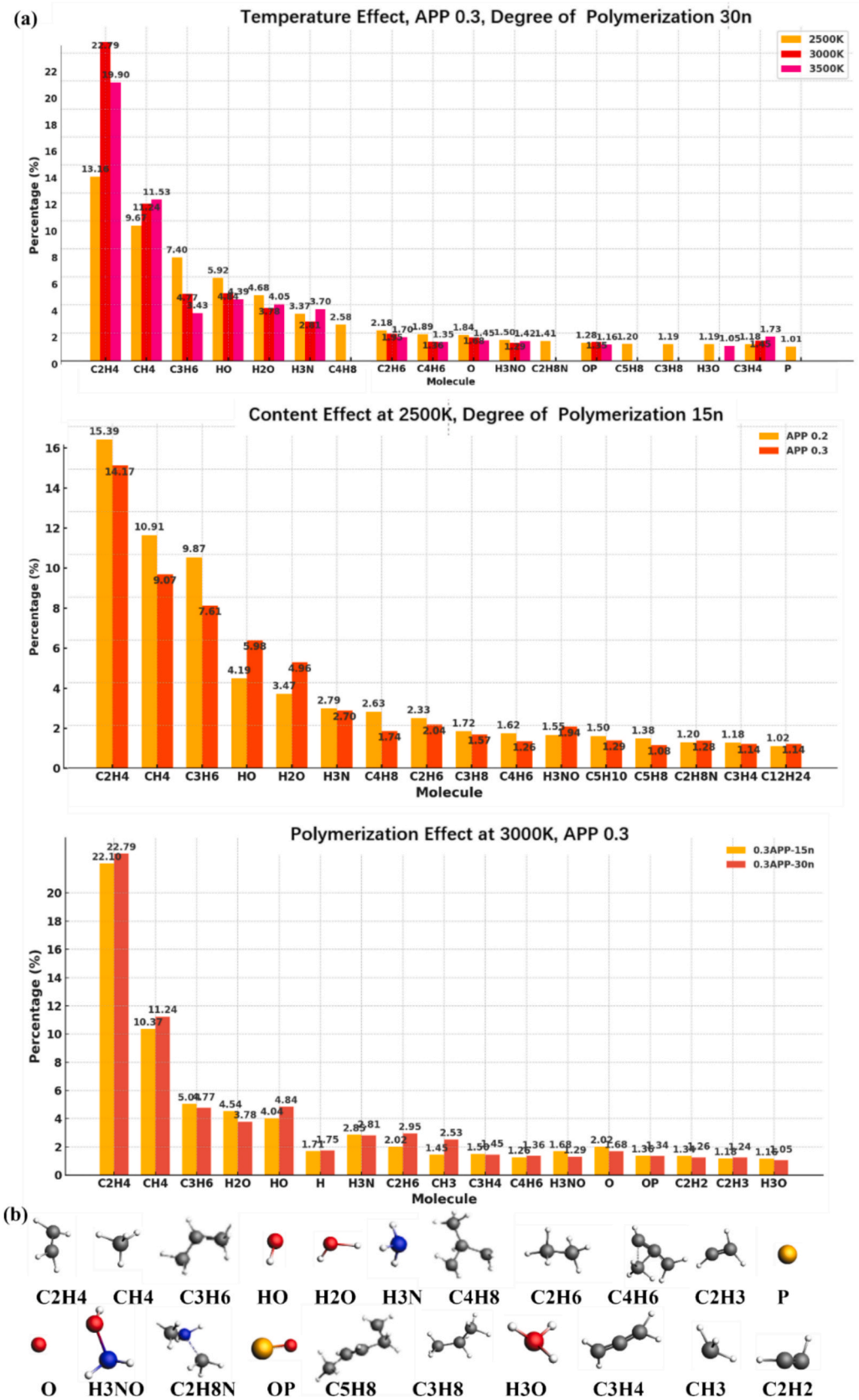

Fig. 13. (a) Effects of temperature, APP content, and polymerisation degree on the distribution of dominant molecules and radicals; (b) representative molecular structures of the identified species.

(typically by 1–2 percentage points) in the mole fractions of C_2H_4, CH_4, C_3H_6 and several minor products. Within the present model, this suggests that at this temperature a higher APP loading can reduce the overall generation of volatile hydrocarbons to some extent. The effect of polymerisation degree is comparatively small (bottom panel). At 3000 K with APP = 0.3, the product distributions of the 15n and 30n systems are very similar: the mole fractions of major species such as C_2H_4 and CH_4 differ by about 1 percentage point or less. This indicates that, for a given temperature and APP content, variations in APP chain length have a weaker influence on the final gas-phase composition than temperature and formulation.

4.8. ReaxFF-MD charaterisation of Phosphate-drive flame retardancy mechanism

ReaxFF-MD was used to extract representative elementary steps from the trajectories (Fig. 14), which are shown as plausible pathways consistent with the simulations and experiments, rather than a complete kinetic mechanism. In the early stage of pyrolysis, nitrogen-containing APP fragments undergo deamination. For example, $C_{12}H_{27}N$ can convert to $C_{12}H_{244}$ with the release of NH_3 (upper part of Fig. 14). The formation of NH_3 is consistent with the intumescent behaviour of the APP systems and provides a source of inert gas during heating. At the same time, a variety of phosphorus–oxygen species are generated. The simulations frequently show PO_2-type fragments and related HO_2P groups, which participate in several classes of reactions. On the one hand, PO_2-containing radicals can react with OH-containing species to form small polyphosphate units such as HO_sP_2 (middle of Fig. 14), which may act as "building blocks" for condensed-phase polyphosphate structures. On the other hand, HO_2P groups can abstract hydrogen atoms from hydrocarbon radicals (e.g. C_2H_s·), yielding saturated molecules such as C_2H_6 and regenerating PO_x species. Such reactions consume combustible radicals and provide a possible route for gas-phase radical quenching. On longer time scales, phosphate fragments interact with larger PP-derived chains. The MD trajectories show that long-chain hydrocarbon fragments (e.g. $C_{46}H_{93}$) can combine with phosphorus-containing intermediates to form P-containing oligomers such as $C_{60}H_{122}O_2P$. Smaller olefins (e.g. C_3H_6, C_9H_{18}) can also add to these phosphorus-containing clusters (bottom of Fig. 14). These processes provide a possible pathway by which unsaturated PP fragments are incorporated into P-rich networks and converted into potential char precursors. Taken together, APP contributes via gas-phase moderation (NH_3 release and PO_x/HO_2P-mediated radical reactions) and condensed-phase stabilisation (P–O–C oligomer growth), consistent with the higher P/N retention, more developed char and reduced hydrocarbon release observed experimentally for WR-APP.

5. Conclusion

In this study, UL-94, LOI, cone calorimetry, TG-FTIR, tensile testing, SEM/EDS, Raman, XPS and ReaxFF-MD were combined to examine how APP polymerisation degree and water solubility affect the fire behaviour of PP/APP composites. The main conclusions are: **(i)** Under the present processing and test conditions, high-polymerisation, low-solubility WR-APP outperforms low-polymerisation, water-soluble WP-APP. WR-APP improves self-extinguishing/anti-dripping at lower loadings (UL-94: V-1 at 30 wt% and V-0 at 50 wt%) and reduces heat/smoke hazards in cone calorimetry (lower pHRR/THR, mass-loss and smoke-related parameters). By contrast, WP-APP remains prone to melt dripping at low–medium loadings, and stable LOI values cannot be obtained under ASTM D2863. **(ii)** The performance differences are accompanied by distinct dispersion- and residue-related features. SEM of unburned composites shows APP accumulations and pull-out cavities that intensify with loading, consistent with the pronounced reductions in ε_max and σ_max. Residue analyses (SEM/EDS, Raman, XPS) indicate stronger P/N retention and higher carbon structural ordering for WR-APP (notably WR-30), whereas WP-APP residues show more cracks/porosity and weaker P/N signals at comparable loadings; 50 wt% residue data are provided in the Supporting Information. **(iii)** ReaxFF-MD reproduces comparative trends in volatile evolution and heavy-fragment growth:

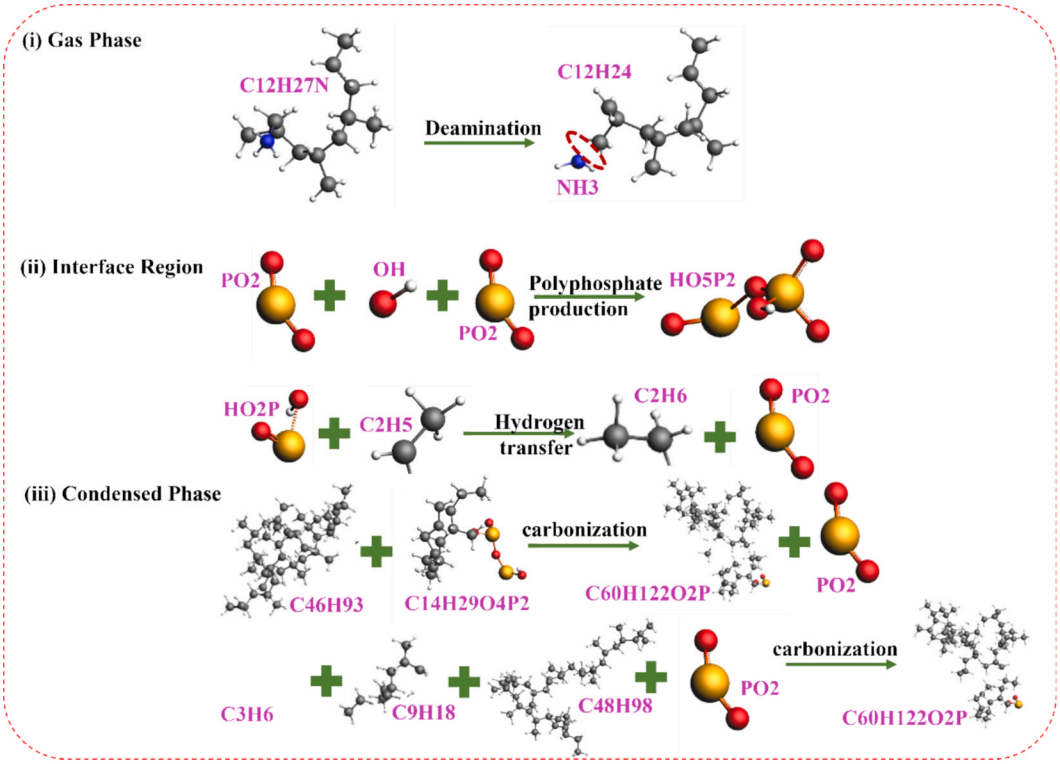

Fig. 14. Schematic representation of the synergistic flame-retardant mechanism in PP/APP composites revealed by ReaxFF-MD.

within 2500–3000 K, increasing APP chain length and loading delays the formation/release of light hydrocarbons and increases the C40 + fraction. Trajectory-derived steps (deamination/NH_3 release, PO_x/HO_2P reactions, and P–O–C oligomer growth) provide plausible pathways for gas-phase radical consumption and condensed-phase phosphate-rich structure development, supported by TG-FTIR observations of evolved volatiles.

Finally, ReaxFF-MD employs elevated temperatures and finite system sizes to access reactions on feasible time scales; thus, the simulation outputs are used to interpret relative mechanisms and trends rather than to directly predict real-temperature kinetics. In addition, this work focuses on within-APP comparisons under identical processing conditions; non-phosphorus flame-retardant controls were not included, and the conclusions should not be interpreted as a cross-chemistry performance ranking among different halogen-free approaches. The conclusions are limited to the two commercial APP grades investigated in this study.

CRediT authorship contribution statement

Chunxiao Liu: Writing – original draft, Visualization, Formal analysis, Data curation, Conceptualization. **Benjamin Tawiah:** Resources, Methodology, Data curation, Conceptualization. **Anthony Chun Yin Yuen:** Writing – review & editing, Supervision, Project administration. **Qian Chen:** Writing – review & editing, Software, Methodology. **Ivan Miguel De Cachinho Cordeiro:** Writing – review & editing, Software. **Yuxin Zhang:** Writing – review & editing. **Liming Jiang:** Writing – review & editing.

Declaration of competing interest

The authors declare that they have no known competing financial interests or personal relationships that could have appeared to influence the work reported in this paper.

Acknowledgements

This work is sponsored by the MTR Research Funding Scheme (PTU-23019) and the PolyU UGC Funding (P0044994) and (P0052426). Also, it is sponsored by the Hong Kong General Research Fund - Early Career Scheme (25200925).

Appendix A. Supplementary data

Supplementary data to this article can be found online at https://doi.org/10.1016/j.compositesa.2026.109610.

Data availability

Data will be made available on request.

References

[1] Chen Z, Han Y, Geng Z. *Novel kinetic modeling strategy for industrial-scale UNIPOL polypropylene with Ziegler-Natta catalyst*. Chem Eng J (Lausanne, Switzerland) 1996;2024(482):148830.
[2] Jordan AM, et al. *Improved Polypropylene Thermoformability through Polyethylene Layering*. ACS Appl Mater Interfaces 2022;14(29):34134–42.
[3] Shen D, et al. *Multifunctional self-powered electronics based on a reusable low-cost polypropylene fabric triboelectric nanogenerator*. ACS Appl Mater Interfaces 2021;13(29):34266–73.
[4] Di X, et al. *Introducing a polysiloxane coating on flame retardant to realize durable UV resistance and flame retardancy of polypropylene*. Polym Degrad Stab 2025;239:111403.
[5] Zheng X, et al. *Tannic acid coated ammonium polyphosphate: for flame retardant and UV resistant of polypropylene*. Polym Degrad Stab 2024;229:110956.
[6] Jin X, et al. *Preparation of a novel intumescent flame retardant based on supramolecular interactions and its application in polyamide 11*. ACS Appl Mater Interfaces 2017;9(29):24964–75.
[7] Ni Y-P, et al. *Semi-aromatic copolyesters with high strength and fire safety via hydrogen bonds and π-π stacking*. Chem Eng J (Lausanne, Switzerland) 1996;2019(374):694–705.
[8] Li S, et al. *In-suit cemented strategy enables intumescent flame retardant transition from hyper-hydrophilic to hydrophobic and aggregation flame retardant effect simultaneously in polypropylene*. Compos B Eng 2024;287:111874.
[9] Liu B-W, et al. *Eco-friendly synergistic cross-linking flame-retardant strategy with smoke and melt-dripping suppression for condensation polymers*. Compos B Eng 2021;211:108664.
[10] Shi X-H, et al. *Flame-retardant strategy and mechanism of fiber reinforced polymeric composite: a review*. Compos B Eng 2022;233:109663.
[11] Zhao W, et al. *Flame retardant treatments for polypropylene: Strategies and recent advances*. Composites Part A, Appl Sci Manuf 2021;145::106382.
[12] Shao Z-B, et al. *A strategy to construct multifunctional ammonium polyphosphate for epoxy resin with simultaneously high fire safety and mechanical properties*. Compos A Appl Sci Manuf 2021;149:106529.
[13] Wu Q, et al. *Toward a new approach to synchronously improve the fire performance and toughness of polylactic acid by the incorporation of facilely synthesized ammonium polyphosphate derivatives*. Compos A Appl Sci Manuf 2021;150:106595.
[14] Chen Y, et al. *The pyrolysis behaviors of phosphorus-containing organosilicon compound modified APP with different polyether segments and their flame retardant mechanism in polyurethane foam*. Compos B Eng 2019;173:106784.
[15] Huang S, et al. *A facile surface modification of ammonium polyphosphate with boron-based compound to reduce its particle size and improve the flame retardancy and anti-dripping of polylactic acid resin*. Colloids Surf A Physicochem Eng Asp 2025;717:136781.
[16] Xie H, et al. *Effect and mechanism of N-alkoxy hindered amine on the flame retardancy, UV aging resistance and thermal degradation of intumescent flame retardant polypropylene*. Polym Degrad Stab 2015;118:167–77.
[17] Chen W-H, et al. *Synchronously enhanced flame retardancy and mechanical properties of polylactic acid via in-situ assembly of polyphosphazene nanoparticles on ammonium polyphosphate*. Chem Eng J (Lausanne, Switzerland) 1996;2024(499):156361.
[18] Wang K, Gao W. *Composite silica aerogel based on HNTs-modified APP with enhanced thermal insulation and flame retardancy performance for organosilicon resin*. Chem Eng J (Lausanne, Switzerland) 1996;2024(497):154804.
[19] Yan Y, et al. *Enhancing the toughness and strength of flame-retardant PLA blends through triglycidyl isocyanurate driven reactive blending*. Chem Eng J (Lausanne, Switzerland) 1996;2025(519):165520.
[20] Zhang Y, et al. *Functionalizing lignin by in situ solid-phase grafting ammonium polyphosphate for enhancing thermal, flame-retardant, mechanical, and UV-resistant properties of polylactic acid*. Chem Eng J (Lausanne, Switzerland) 1996;2024(495):153429.
[21] Lim K-S, et al. *A review of application of ammonium polyphosphate as intumescent flame retardant in thermoplastic composites*. Compos B Eng 2016;84:155–74.
[22] Sun Y, et al. *Surface modification of ammonium polyphosphate by supramolecular assembly for enhancing fire safety properties of polypropylene*. Compos B Eng 2020;181:107588.
[23] Yang H, et al. *Synergistic effect of nanoscale carbon black and ammonium polyphosphate on improving thermal stability and flame retardancy of polypropylene: a reactive network for strengthening carbon layer*. Compos B Eng 2019;174:107038.
[24] Wang N, et al. *Influence of mesoporous fillers with PP-g-MA on flammability and tensile behavior of polypropylene composites*. Compos B Eng 2013;44(1):467–71.
[25] Wang X, Gao Y, Chu G. *Optimization and characterization of polyphosphate fertilizers by two different manufacturing processes*. ACS Omega 2021;6(29):18811–22.
[26] Wang B, et al. *One-Pot Synthesis and Hydrolysis Behavior of Highly Water-Soluble ammonium Polyphosphate*. ACS Sustain Chem Eng 2022;10(39):13037–49.
[27] Yuan H, et al. *Stable preparation of highly water-soluble ammonium polyphosphate by ion regulation*. Chemical engineering journal (Lausanne. Switzerland 1996;2023(467):143437.
[28] Schartel B, Hull TR. *Development of fire-retarded materials-Interpretation of cone calorimeter data*. Fire Mater 2007;31(5):327–54.
[29] Morgan AB, Gilman JW. *An overview of flame retardancy of polymeric materials: application, technology, and future directions*. Fire Mater 2013;37(4):259–79.
[30] Camino G, Costa L, Luda di Cortemiglia MP. *Overview of fire retardant mechanisms*. Polym Degrad Stab 1991;33(2):131–54.
[31] He F-M, et al. *Novel polyamide 6 composites based on Schiff-base containing phosphonate oligomer: High flame retardancy, great processability and mechanical property*. Compos A Appl Sci Manuf 2021;146:106423.
[32] Liu L, et al. *Preparation of phosphorus-doped chitosan derivative and its applications in polylactic acid: Crystallization, flame retardancy, anti-dripping and mechanical properties*. Int J Biol Macromol 2024;265(Pt 1):130648.
[33] Xu B, et al. *Synthesis and characterization of a novel organic-inorganic hybrid char-forming agent and its flame-retardant application in polypropylene composites*. J Anal Appl Pyrol 2018;134:231–42.
[34] Yuen A, et al. *Utilising genetic algorithm to optimise pyrolysis kinetics for fire modelling and characterisation of chitosan/graphene oxide polyurethane composites*. Compos B Eng 2020;182:107619.
[35] Yuen ACY, et al. *Developing a solid decomposition kinetics extraction framework for detailed chemistry pyrolysis and combustion modelling of building polymer composites*. J Anal Appl Pyrol 2022;163:105500.
[36] Car R, Parrinello M. *Unified approach for molecular dynamics and density-functional theory*. Phys Rev Lett 1985;55(22):2471–4.
[37] Senftle TP, et al. *The ReaxFF reactive force-field: development, applications and future directions*. npj Computational Materials 2016;2:15011.

[38] De Cachinho Cordeiro IM, et al. *Pyrolysis and combustion characterisation of HDPE/APP composites via molecular dynamics and CFD simulations*. J Anal Appl Pyrol 2022;163:105499.
[39] Wang X-F, et al. *Construction of phytic acid-based composite self-assembled coatings to improve the flame retardant and smoke inhibition properties of polystyrene*. Int J Biol Macromol 2025;319(Pt 4):145526.
[40] Li J-F, Jiang W, Gao Y. *Synergistic P-N charring agents to enhance flame retardancy of ethylene-vinyl acetate (EVA): Insights from experimental and molecular dynamic simulations*. Polym Degrad Stab 2023;218:110570.
[41] van Duin ACT, et al. *ReaxFF: A Reactive Force Field for Hydrocarbons*. Journal of Physical Chemistry. A, Molecules, Spectroscopy, Kinetics, Environment & General Theory 2001;105(41):9396–409.
[42] Chenoweth K, van Duin ACT, Goddard WA. *ReaxFF Reactive Force Field for Molecular Dynamics Simulations of Hydrocarbon Oxidation*. J Physical Chemistry A, Molecules, spectroscopy, kinetics, environment, & general theory 2008;112(5):1040–53.
[43] Martínez L, et al. *PACKMOL: a package for building initial configurations for molecular dynamics simulations*. J Comput Chem 2009;30(13):2157–64.
[44] Li J, et al. *A Molecular Understanding of the Flame Retardant Mechanism of Zinc Stannate/Polypropylene Composites via ReaxFF Simulations*. Inorganics 2023;11(6):233.
[45] Vaari J, Paajanen A. *Evaluation of the reactive molecular dynamics method for Research on flame retardants: ATH-filled polyethylene*. Comput Mater Sci 2018;153:103–12.
[46] De Cachinho Cordeiro IM, et al. *Characterising flame-retardant mechanism of phosphorous-containing intumescent coating on polyethylene via ReaxFF MD simulations*. Chem Eng J (Lausanne, Switzerland) 1996;2024(480):148169.
[47] Salmeia KA, et al. *Comprehensive study on flame retardant polyesters from phosphorus additives*. Polym Degrad Stab 2018;155:22–34.
[48] Arvelos S, Abrahão O, Eponina Hori C. *ReaxFF molecular dynamics study on the pyrolysis process of cyclohexanone*. J Anal Appl Pyrol 2019;141:104620.
[49] Zheng WT, et al. *Nitrogen 1s electron binding energy assignment in carbon nitride thin films with different structures*. J Electron Spectrosc Relat Phenom 1997;87(1):45–9.
[50] Sun B, et al. *Structure–tuned, phosphorus–doped hierarchical porous biochar via green hydrothermal carbonization and activation for formaldehyde adsorption*. Fuel (Guildford) 2026;404:136381.